Environmental Science & Technology

pubs.acs.org/est

Article

Using High-Temporal-Resolution Ambient Data to Investigate Gas-Particle Partitioning of Ammonium over Different Seasons

Qianyu Zhao, Athanasios Nenes, Haofei Yu, Shaojie Song, Zhimei Xiao, Kui Chen, Guoliang Shi,* Yinchang Feng, and Armistead G. Russell

Cite This: *Environ. Sci. Technol.* 2020, 54, 9834−9843

Read Online

ACCESS | Metrics & More | Article Recommendations | Supporting Information

ABSTRACT: Ammonium is one of the dominant inorganic water-soluble ions in fine particulate matter ($PM_{2.5}$). In this study, source apportionment and thermodynamic equilibrium models were used to analyze the relationship between pH and the partitioning of ammonium ($\varepsilon(NH_4^+)$) using hourly ambient samples collected from Tianjin, China. We found a "Reversed-S curve" between pH and $\varepsilon(NH_4^+)$ from the ambient hourly aerosol dataset when the theoretical $\varepsilon(NO_3^-)$* (an index identified in this work) was within specific ranges. A Boltzmann function was then used to fit the Reversed-S curve. For the summer data set, when $\varepsilon(NO_3^-)$* was between 0.7 and 0.8, the fitted R^2 was 0.88. Through thermodynamic analysis, we found that the values of $k[H^+]^2$ (k = 3.08 × 10^4 L^2 mol^{-2}) and $\varepsilon(NO_3^-)$* can influence the pH-$\varepsilon(NH_4^+)$ curve. Under certain situations, the values of $k[H^+]^2$ and $\varepsilon(NO_3^-)$* are similar to each other, and $\varepsilon(NH_4^+)$ is sensitive to pH, suggesting that $\varepsilon(NO_3^-)$* plays an important role in affecting the $\varepsilon(NH_4^+)$. During summer, winter, and spring seasons, when the relative humidity was greater than 0.36 and $\varepsilon(NO_3^-)$* was between 0.8 and 0.95, there was an obvious Reversed-S curve, with R^2 = 0.60. The theoretical $k[H^+]^2$ and $\varepsilon(NO_3^-)$* developed in this work can be used to analyze the gas-particle partitioning of ammonia−ammonium and nitrate−nitric acid in the ambient atmosphere. Also, it is the first time that we created the joint source-NH_3/HNO_3 maps to integrate sources, aerosol pH and liquid water content, and ions (altogether in one map), which can provide useful information for designing effective strategies to control particulate matter pollution.

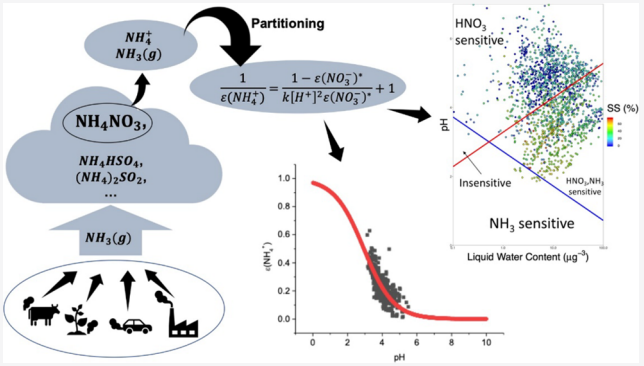

INTRODUCTION

Ammonium, nitrate, and sulfate are commonly found to be the dominant inorganic components of $PM_{2.5}$ in China.[1−4] The results from previous studies have shown that these water-soluble ions (WSI) are generated from secondary formation.[5,6] Ammonium and nitrate are semivolatile species[7−9] subject to gas-particle partitioning processes, and research has shown that acidity and meteorological conditions play important roles in such processes.[8,10,11,44]

The past literature suggests a "Reversed-S curve" (Figure S1a) relationship between the partitioning of ammonium (expressed as $\varepsilon(NH_4^+)$: $[NH_4^+]/([NH_3(g)] + [NH_4^+])$) and pH in aerosols and cloud droplets and an "S curve" relationship between the partitioning of nitrate (expressed as $\varepsilon(NO_3^-)$: $[NO_3^-]/([HNO_3(g)] + [NO_3^-])$) and pH.[12] However, these results were mostly obtained within laboratory environments and were designed to simulate the conditions in clouds. Studies on the relationship between $\varepsilon(NO_3^-)$ and pH in ambient aerosol are limited. In ambient aerosol, the relationship between gas-particle partitioning of semivolatile WSI and pH may be influenced by many factors, such as the fluctuation of temperature (T), relative humidity (RH), water content in aerosol, and source emissions.[12]

In our previous study, by using an hourly ambient aerosol data set, we found an S curve relationship between $\varepsilon(NO_3^-)$ and pH under actual atmospheric conditions. The partitioning of nitrate in ambient aerosols is found to be influenced by meteorological conditions (T, RH) and the strength of source emissions.[9] The S curve and Reversed-S curve can be applied to divide the entire range of pH into sensitive band, upper band, and lower band (Figure S1). For the sensitive band, $\varepsilon(NH_4^+)$ and $\varepsilon(NO_3^-)$ vary markedly with an increase in pH; for the upper band, $\varepsilon(NH_4^+)$ and $\varepsilon(NO_3^-)$ approach 1; while for the lower band, $\varepsilon(NH_4^+)$ and $\varepsilon(NO_3^-)$ approach 0. Nenes et al. created sensitivity maps according to the theoretical S curve to divide the regions into a nitrate-sensitive region,

Received: December 2, 2019
Revised: July 16, 2020
Accepted: July 17, 2020
Published: July 17, 2020

ammonium-sensitive region, both nitrate- and ammonium-sensitive regions, and nonsensitive region.[12,13] Also, in our study of aerosol pH, the sensitivities of HNO_3 and NH_3 partitioning are different in different zones.[13] However, the synergistic influence of HNO_3 and NH_3 is still not clear. In this work, we further investigate the relationship between $\varepsilon(NH_4^+)$, $\varepsilon(NO_3^-)$, and pH in ambient aerosol and explore the factors that affect such relationships.

Compared with $\varepsilon(NO_3^-)$, the response of $\varepsilon(NH_4^+)$ to various meteorological and compositional factors may be more complex. In the ambient atmosphere, ammonium can react with both nitrate and sulfate.[14−16] Owing to its extremely low volatility, the acidic H_2SO_4 resides in the aerosol phase and reacts with $NH_3(g)$ from the gas phase to form secondary ammonium sulfate/bisulfate.[17] If sufficient amounts of ammonia are present, $HNO_3(g)$ can react with NH_3 to form ammonium nitrate (NH_4NO_3),[9] with the equilibrium between NH_4NO_3, NH_3, and HNO_3 being very temperature and humidity sensitive.[17−19] Thus, to investigate the relationship between $\varepsilon(NH_4^+)$ and pH in the ambient atmosphere, the presence of $\varepsilon(NO_3^-)$, SO_4^{2-}, and the influence of varying environmental conditions such as T and RH should be analyzed. Additionally, sources such as coal, dust, and vehicle can attribute cations and anions to aerosol and emit precursor gases such as NH_3, SO_2, NO_x, etc. Therefore, source impacts should also be considered as potential influencing factors to the $\varepsilon(NH_4^+)$−pH relationship.

In this study, the relationship between $\varepsilon(NH_4^+)$ and pH in ambient atmosphere is investigated. The research presented here is based on our previous work,[9] in which we explored the impact factors on $\varepsilon(NO_3^-)$ and pH in the ambient atmosphere. In this work, an hourly data set was collected during summer, winter, and spring from a northern city in China. The positive matrix factorization (PMF)/multilinear engine program (ME2) source apportionment model was used to explore source emission patterns. The thermodynamic model (ISORROPIA-II) was applied to estimate the hourly aerosol pH to analyze the relationship between pH and $\varepsilon(NH_4^+)$ partitioning. Then, the impacts of meteorological parameters, inorganic ion concentration, source emissions, and $\varepsilon(NO_3^-)$ on aerosol pH and $\varepsilon(NH_4^+)$ were explored. The relationships between pH and $\varepsilon(NH_4^+)$ were described by a sigmoid function, and the impacts of different factors were discussed based on the results of thermodynamics analysis. What's more, to explore the relationship between ambient NH_4^+/NH_3 and NO_3^-/HNO_3, the $\varepsilon(NH_4^+)$ and $\varepsilon(NO_3^-)$ were discussed together. Finally, the joint source-NH_3/HNO_3 sensitivity regime maps were created, to better understand the formation of secondary nitrate. These maps are powerful because they integrate sources, pH and liquid water content (LWC), and PM sensitivity to NH_3/HNO_3 emissions in one map. The findings of this work contribute to a better understanding of inorganic secondary aerosol formation. Additionally, the sensitivity regime maps help establish the relationships between primary sources (coal, dust, and vehicle) and secondary sources (secondary nitrate (SN) and secondary sulfate (SS)), which can provide useful information for designing effective strategies to control particulate matter pollution.

METHODS

Sampling and Chemical Analysis. Online aerosol and gas measurements with 1 h temporal resolutions were conducted in the megacity of Tianjin, China, in summer, spring, and winter. The sample collection location is in a community located about 200 meters away from a major road with heavy traffic congestion. The URG9000B Ambient Ion Monitor (AIM, URG Corporation, Chapel Hill, NC.) with two ICs was used to measure water-soluble ions, including NH_4^+, Na^+, K^+, Ca^{2+}, Mg^{2+}, SO_4^{2-}, NO_3^-, Cl^-, F^-, NO_2^-, and semivolatile species in the gas phase, including HCl, HNO_3, and NH_3. Details of the sampling method and time period are described in our prior work.[9]

pH Prediction. pH is a basic property of the aqueous fraction of an aerosol. It is determined by H^+, liquid water content, and ion activity of H^+.[8,14] Because there is no method to directly measure the acidity of aerosols, scholars generally use thermodynamic analysis of the components in aerosols to estimate the acidity.[21−29] In this study, the samples were introduced into ISORROPIA-II (http://nenes.eas.gatech.edu/ISORROPIA/index_old.html or https://isorropia.epfl.ch) to estimate the aerosol pH (eq 1) as well as gas-particle partitioning of water-soluble ions, semivolatile substances, and water content.[29−32] In total, 387 hourly samples were introduced. The input data included meteorological parameters (temperature and relative humidity), concentrations of water-soluble ions, and concentrations of semivolatile components. In the samples, RH ranged from 47.2 to 79.4%, with average values of 60.1%. In ISORROPIA-II, forward mode and metastable mode were selected. In the forward mode, known quantities include temperature, relative humidity, and total concentrations of $NH_4^+/NH_3(g)$, SO_4^{2-}, Cl^-, $NO_3^-/HNO_3(g)$, Na^+, K^+, Ca^{2+}, and Mg^{2+}. In the metastable mode, there is no precipitation under supersaturated conditions.[9,33,34]

Aerosol pH as calculated in ISORROPIA-II is

$$\mathrm{pH} = -\log_{10}\left(\frac{m_{H^+} \times 1000}{\text{water content}}\right) \quad (1)$$

where m_{H^+} is the concentration ($\mu g\ m^{-3}$) of H^+.[8,20,34] The unit of water content is $\mu g\ m^{-3}$. The molarity-based activity coefficient of hydrogen ions is assumed to be unity in ISORROPIA-II.[22]

Extended AIM Aerosol Thermodynamic Model (E-AIM). In this work, E-AIM was used to estimate the activity coefficients of different ions in aerosol (http://www.aim.env.uea.ac.uk/aim/aim.php). There are four models in E-AIM: model I (H^+−SO_4^{2-}−NO_3^-−Cl^-−Br^-−H_2O, <200 to 330 K), model II (H^+−NH_4^+−SO_4^{2-}−NO_3^-−H_2O, <200 to 330 K), model III (H^+−NH_4^+−SO_4^{2-}−NO_3^-−Cl^-−H_2O, at 298.15 K only), and model IV (H^+−NH_4^+−SO_4^{2-}−NO_3^-−Cl^-−H_2O, ≤263 to 330 K). In this study, the data sets of aerosols we collected included ammonium, sulfate, nitrate, and chloride. Thus, the activity coefficients of ions in the aerosols were obtained by E-AIM model IV. Because E-AIM model IV requires RH > 60%,[34] only samples with an RH larger than 60% were introduced to E-AIM.

Source Apportionment: Positive Matrix Factorization (PMF)/Multilinear Engine 2 (ME2). Multivariate receptor modeling of time-series data sets is often used to perform source apportionment of the airborne particulate matter.[35,36] The PMF model is one of the two independent and complementary source apportionment models that were developed by the U.S. EPA (Environmental Protection Agency) (the other being Unmix). We choose the PMF model, using the ME2 solver,[36,37] to estimate source

https://dx.doi.org/10.1021/acs.est.9b07302
Environ. Sci. Technol. 2020, 54, 9834−9843

contributions in this study because based on our experience, the results obtained from the Unmix model can sometimes be problematic.[38] Details on PMF/ME2 model are shown in the Supporting Text I.

RESULTS AND DISCUSSION

Concentrations and Sources for Ions. pH is one of the critically important properties of aerosols. Processes related to gas-aerosol partitioning and chemical composition are driven by the pH of aerosol.[30,39−44] The pH of aerosol also impacts gas-particle partitioning of the nitrogen cycle, including HNO_3−NO_3^- and NH_3−NH_4^+.[24] To better investigate the relationship between NH_4^+/NH_3 and pH, we first study the summer dataset and then compare the results with those of spring and winter. The NH_3(g) concentration in summer ranged from 13.8 to 37.5 $\mu g\ m^{-3}$, with an average of 25.6 $\mu g\ m^{-3}$. The concentrations of NH_4^+ ranged from 3.2 to 27.5 $\mu g\ m^{-3}$, with an average of 14.0 $\mu g\ m^{-3}$. The mean ambient temperature was 301.4 K (298.2−303.8 K), and mean RH was 60.1% (47.2−79.4%). By applying the ISORROPIA-II model, values of aerosol pH in summer were obtained. Aerosol pH ranged from 2.6 to 4.6 (average value is 3.4). The diurnal variations of ion concentrations, pH, and meteorological conditions can be found in our previous work.[9]

Seasonal and emission-driven variations play an important role in affecting air pollutants' concentrations in the ambient dataset.[45] PMF/ME2 was used to identify the potential source categories and to estimate their contributions in the summer samples. In this study, a sample matrix (387 × 12) was introduced to PMF/ME2. Source profiles and source contributions are provided in Figure S2. Five sources were identified.

Factor 1 has a high SO_4^{2-}, a known marker for secondary sulfate (SS). In summer, factor 2 was characterized by NO_3^-, which is the marker for secondary nitrate (SN). Factor 3 can be identified as dust, as characterized by the high Ca^{2+}.[46] Factor 4 was characterized by the high OC and EC fractions, which are associated with vehicle exhaust.[47] Factor 5 was relevant to coal combustion, as identified by the high OC, EC, Cl^-, and secondary sources (SO_4^{2-}, NO_3^-, NH_4^+).[5] The detailed source profiles are shown in Figure S2. In this work, contributions from different sources to $PM_{2.5}$ were also calculated, and the average contributions were SS (25%), SN (23%), dust (22%), vehicle (13%), and coal (17%). Further information on the source apportionment method was provided in our previous work.[9]

Variations of NH_4^+ and NH_3(g). Ammonia, the most abundant basic gas in the atmosphere, can react with H_2SO_4 and HNO_3 to form ammonium salts.[48] Here, we first investigated the relationship between NH_4 and NH_3. Figure 1 shows the correlations between NH_4^+, NH_3(g), and pH in summer. No clear linear relationship between NH_4^+ and NH_3(g) can be observed, which is expected. Generally, the relationship between ammonia and ammonium should be nonlinear, because the relationship is influenced by many factors such as pH, effective Henry's constant, liquid water content, etc.[12]

Sources such as fossil fuel combustion and vehicle have a significant impact on ammonia.[49,50] Some sources directly emit ammonia and ammonium into the air, while some sources indirectly influence the partitioning of ammonium by emitting cations and anions that influence the pH. To explore the impacts of sources on NH_4^+/NH_3(g), the calculated source

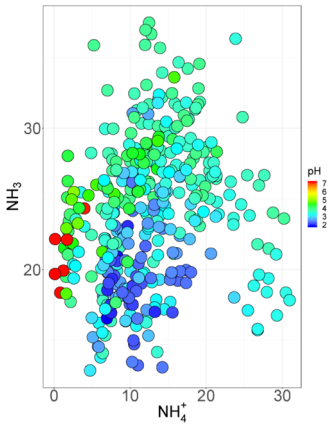

Figure 1. Comparison of mass concentrations of NH_3(g) and NH_4^+ ($\mu g/m^3$) and their relationships with pH in summer.

contributions were set as the third dimension in NH_4^+ vs NH_3(g) plots, as shown in Figure S3a−e. In the results obtained from the summer dataset, coal contributions were generally higher when NH_4^+ was at higher levels, indicating that coal (residential and industrial coal combustion) is likely related to NH_4^+ formation (Figure S3c). In northern China, coal combustion plays an important role in industries. Coal combustion and industrial activities contribute to the emission of NH_3(g),[6] which may explain the relation between coal contributions and NH_4^+. Dust and vehicle showed no obvious impact patterns on NH_4^+/NH_3(g) plots (Figure S3d,e). Interestingly, SS became higher when NH_4^+ was at a moderate level, and SN showed a high level when NH_4^+ was also at a high level (Figure S3a,b). This finding suggests that when sufficient NH_4^+ was available, NH_4^+ would preferably react with sulfate and then with nitrate.[12,51]

In addition to source contributions, meteorological conditions, ion concentrations, aerosol pH, and partitioning of nitrate were also set as the third dimension of the NH_4^+−NH_3(g) plots in summer, and the results are shown in Figure S4a−e. In Figure S4a,e, temperature and gas-particle partitioning of nitrate shows nonlinear impacts on either NH_4^+ or NH_3(g). When the RH was high, as shown in Figure S4b, both concentrations of NH_4^+ or NH_3(g) were high. The concentrations of SO_4^{2-} and NO_3^- were high when NH_4^+ was high. However, none of the variables in the figure show any apparent linear relationships between NH_4^+ and NH_3(g).

Impact of pH on $\varepsilon(NH_4^+)$. The results from our previous work show that the gas-particle partitioning of ammonium salts in the aerosol is mainly driven by its precursors' thermodynamic states and meteorological conditions.[48] The interactions between pH and gas-particle partitioning of ammonia were studied here. The values of $\varepsilon(NH_4^+)$ (calculated as $[NH_4^+]/([NH_3(g)] + [NH_4^+])$) in summer ranged from 0.06 to 0.64, with an average of 0.34. Under atmospheric conditions, practically all dissolved ammonia in the liquid phase is in the form of ammonium ion. The gas-particle partitioning of ammonia has a functional relationship dictated by Henry's law constant.[12] Henry's law constant is impacted by $[H^+]$, which also determines the pH.[12] Thus, the NH_4^+/NH_3(g) is expected to have the following relationship with pH and Henry's law constant as follows[12]

https://dx.doi.org/10.1021/acs.est.9b07302
Environ. Sci. Technol. 2020, 54, 9834−9843

$$[NH_4^+] = \frac{H_{NH_3} K_{a1} [H^+]}{K_w} p_{NH_3} \quad (2)$$

In eq 2, H_{NH_3} is Henry's law constant for ammonia, M atm^{-1}. K_{a1} is the equilibrium constant of the reaction $NH_3 \cdot H_2O \leftrightarrow NH_4^+ + OH^-$. $[H^+]$ is the concentration of H^+. K_w is the equilibrium constant of the reaction $H_2O \leftrightarrow H^+ + OH^-$. pNH_3 is the partial pressure of $NH_3(g)$.

For an $NH_4^+ - NH_3(g)$ system inside cloud, under constant T and RH, a Reversed-S curve relationship between particle-gas partitioning of semivolatile species ($\varepsilon(NH_4^+)$) and aerosol pH (see Figure S1a) is expected. If the Reversed-S curve is found, the curve can be applied to estimate the aerosol pH given available measurements of $\varepsilon(NH_4^+)$. The Reversed-S curve was derived using a sigmoid function, which is a bounded differentiable real function.[52] The Reversed-S curve characterizes a process that starts at a large value, then shows an accelerated decreasing trend, and finally approaches zero: the acceleration portion of the Reversed-S curve is usually in the middle; the other two regions are defined as insensitive regions. In our study, the Reversed-S curve is not only used to estimate the aerosol pH but also provides a method to divide the sensitivity regions of pH. There are three regions in Figure S1a. Region (1) and (3) are pH-insensitive bands (upper and lower bands), where $\varepsilon(NH_4^+)$ changes only slightly with respect to pH change. Region (2) is a pH-sensitive band, where $\varepsilon(NH_4^+)$ drops drastically with pH increase. It should be noted that under ambient conditions, the Reversed-S curve might be less obvious because of two reasons: first, other cation/anions (SO_4^-, NO_3^-, Ca^{2+}, etc.) might influence the $NH_4^+/NH_3(g)$ system; second, T, RH, and ionic activity coefficients do not remain constant in real environmental samples. We plotted $\varepsilon(NH_4^+)$ (calculated from the measured mole concentration of NH_4^+ and $NH_3(g)$) against aerosol pH. At first glance, no obvious Reversed-S curve between $\varepsilon(NH_4^+)$ and pH can be observed. In our previous research, an S curve relationship was found between $\varepsilon(NO_3^-)$ (gas-particle partitioning of NO_3^-) and pH for ambient samples under certain conditions. We also found that the relationship between pH and $\varepsilon(NO_3^-)$ is influenced by $I_{TL}^{HNO_3}$ (an index related to T and RH. $I_{TL}^{HNO_3}$ is defined as $3.2RTL$, where R is the ideal-gas constant, T is the temperature in K, and L is the cloud/fog liquid water content in g m^{-3}), $[H^+]$, and pollution sources.[9] Here, we applied a similar approach to analyze the influences of pollution sources and meteorological conditions on the relationship of pH$-\varepsilon(NH_4^+)$.

Impact of Sources, Meteorological Conditions, and Ion Activity on pH-$\varepsilon(NH_4^+)$. Five three-dimensional scatter plots on the impacts of SN, SS, coal, vehicle, and dust source on the pH$-\varepsilon(NH_4^+)$ relationship are provided in Figure S5a–e. In summer, SS increases significantly when $\varepsilon(NH_4^+)$ is above 0.1 and between a pH of 2 and 3.5 (Figure S5b). This is because the relative abundances of $(NH_4)_2SO_4$ and NH_4HSO_4 are related to the amount of NH_4^+, particularly under high SS conditions. SN begins to increase when $\varepsilon(NH_4^+)$ is above 0.3 and in the region where the pH is between 3 and 4 (Figure S5a). Such a result suggests that ammonia reacts with sulfate ions first (at a relative low pH level) and then with nitrate (at a moderate pH level).[12,51] In Figure S5c–e, dust and vehicle show no clear relationships with pH$-\varepsilon(NH_4^+)$, and the coal source is generally dominant at higher $\varepsilon(NH_4^+)$ (>0.4) and moderate pH (4–5) levels. The results from our previous study also showed that coal was the main source of ammonium ions and at moderate pH levels.[12,51] Based on the analysis above, it can be seen that secondary aerosol (SS and SN) can influence the pH$-\varepsilon(NH_4^+)$ relationship significantly, while the influence of other primary sources (coal dust and vehicle) is less clear. However, though SS and SN have a great impact on pH and $\varepsilon(NH_4^+)$, their influence is nonlinear because of chemical behaviors.[51] Other sources influence $\varepsilon(NH_4^+)$ and pH indirectly by emitting ions into the atmosphere, which is also nonlinear. Overall, the impact of source contributions on the $\varepsilon(NH_4^+)-$pH relationship was nonlinear.[53]

Aerosol is able to absorb a large amount of water, which has a significant impact on its chemical and physical properties.[54] The effects of temperature and RH on the pH$-\varepsilon(NH_4^+)$ relationship were also explored here (Figures S6 and S7). In summer, a higher temperature is associated with lower pH (<3). The reason is that when the temperature increases, the equilibrium of the reaction $NH_3(g) + H_2O \rightleftharpoons NH_4^+ + OH^-$ shifts to the left, thus increasing the gaseous NH_3. The impact of RH on the pH$-\varepsilon(NH_4^+)$ relationship in summer is provided in Figure S7. It appears that samples taken at a high RH (>60%) are primarily located in the regions of the sensitive band of the Reversed-S curve (Figure S1a). Additionally, a higher RH is related to higher $\varepsilon(NH_4^+)$. The reason is that when the relative humidity rises, the water content in the air increases, resulting in more ammonia gas dissolving in water.[12] RH is a key factor of aerosol water content. We also investigated the impact of water content (calculated by ISORROPIA-II) onto $\varepsilon(NH_4^+)$ and $\varepsilon(NH_4^+)$* (partitioning of ammonium calculated by ISORROPIA-II) (Figure S8). In summer, higher water content is generally related to high $\varepsilon(NH_4^+)$, due to the fact that when aerosol water content increases, the dissolution of ammonium increases. Unlike RH, no obvious sensitive band was found at the high-water-content points in the plot. However, water content is still an important property of aerosol, because it serves as the reservoir for reactions to occur in aerosol.[55−57]

The phase equilibria and gas-particle partitioning are influenced by the nonideality of the liquid phase. Thus, activity coefficients should be considered.[58−61] To further study the influence of the ions, the E-AIM Model IV was used to estimate ion activity coefficients. As shown in related studies,[34] E-Aim Model IV is more accurate when RH is above 60%. Therefore, only sample measurements with RH greater than 60% from the summer data sets were input into E-Aim Model IV. The results are shown in Figure S9. In summer, $\log \gamma(SO_4^{2-})$ was higher at moderate pH levels and lower at low and high pH levels, while $\log \gamma(NO_3^-)$, $\log \gamma(H^+)$, and $\log \gamma(NH_4^+)$ were lower at moderate pH levels and higher at low and high pH levels. In addition, when $\varepsilon(NH_4^+)$ was at higher levels, $\log \gamma(NH_4^+)$ was higher and $\log \gamma(SO_4^{2-})$ was lower. This result also suggested that the pH$-NH_4^+/NH_3$ was driven by nonlinear chemistry.[53]

Relationship between pH, $\varepsilon(NH_4^+)$, and $\varepsilon(NO_3^-)$. As previously discussed, $\varepsilon(NH_4^+)$ was significantly influenced by SS and SN. The reasons for this are due to the affinity of NH_4^+ to both SO_4^{2-} and NO_3^- in the formation of $(NH_4)_2SO_4$ and because NH_4NO_3 and NH_4NO_3 are semivolatile.[9,51] In the atmosphere, gas-phase NH_3 mainly comes from emissions, but it can also evolve from the decomposition of NH_4NO_3, which is formed through the reaction $NH_4^+ + NO_3^- \rightleftharpoons NH_4NO_3$. Thus, the phase distribution of nitrate is important to understanding the value of $\varepsilon(NH_4^+)$.[62] For NH_4^+ and NO_3^-,

https://dx.doi.org/10.1021/acs.est.9b07302
Environ. Sci. Technol. 2020, 54, 9834−9843

the study of $\varepsilon(NH_4^+)$ also considers the relationship between gas-particle partitioning of NH_4^+ and NO_3^-. It is also necessary to pay attention to the influence of $\varepsilon(NO_3^-)$ on the relationship between pH and $\varepsilon(NH_4^+)$. As shown in our previous work and previous literature,[9,12] theoretical $\varepsilon(NO_3^-)$ can be calculated from pH, temperature, and water content. In this work, we defined the theoretical $\varepsilon(NO_3^-)$ as $\varepsilon(NO_3^-)$*, which can be calculated by eq 3[9]

$$\varepsilon(NO_3^-)^* = \frac{10^{-6} H_{HNO_3} RTL}{1 + 10^{-6} H_{HNO_3} RTL} \quad (3)$$

where R is the ideal-gas constant 0.08205 (atm L mol^{-1} K^{-1}), T is the temperature in K, and L is the cloud/fog liquid water content in g m^{-3}.

In Figure 2, the relationship between $\varepsilon(NH_4^+)$, pH, and $\varepsilon(NO_3^-)$* is shown for summer. As $\varepsilon(NO_3^-)$* was high, the

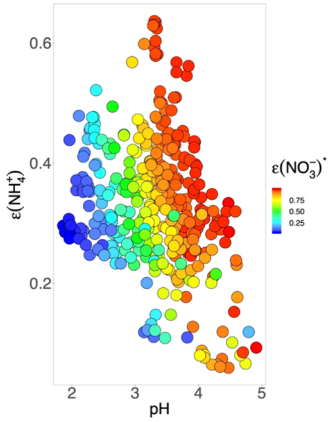

Figure 2. $\varepsilon(NH_4^+)$ as a function of pH, filled with $\varepsilon(NO_3^-)$* in summer.

expected Reversed-S curve was observed, indicating that $\varepsilon(NH_4^+)$ has a more prominent relationship with pH when $\varepsilon(NO_3^-)$* is constrained within a certain range.

To analytically describe the relationship between $\varepsilon(NH_4^+)$ ratio and pH under certain $\varepsilon(NO_3^-)$* ratios, a Boltzmann equation was applied to fit a regression curve for pH−$\varepsilon(NH_4^+)$ for summer samples. The Boltzmann equation can be used to fit a sigmoid-shaped curve and has performed well in the previous works.[9,63,64] The Origin 8.5 software was employed to perform the curve fitting and the result of the summer data set is shown in Figure 3a. The fitted curves are shown in Figure 3a, with $\varepsilon(NO_3^-)$* constrained between 0.7 and 0.8. The R^2 is 0.88, which suggested a good Reversed-S curve relationship

$$\varepsilon(NH_4^+) = \frac{1}{1 + e^{pH-2.84/0.60}}, \quad R^2 = 0.88 \quad (4)$$

The expected values of $\varepsilon(NH_4^+)$ ratios as predicted by the above regression equations (red lines in Figure 3a, simulated by eq 4) were also calculated accordingly using Origin. The extrapolated data are shown as the red points and the actual ambient sample data are shown as the black points. The results show that the collected ambient samples (black points) were in the pH−$\varepsilon(NH_4^+)$ sensitive region, indicating that a small change of aerosol pH would have a considerable impact on $\varepsilon(NH_4^+)$ (Figure 3a). Nonetheless, there are still a few black points that deviate from the fitted Reversed-S curve, possibly due to uncertainties involved in the curve fitting and analytical

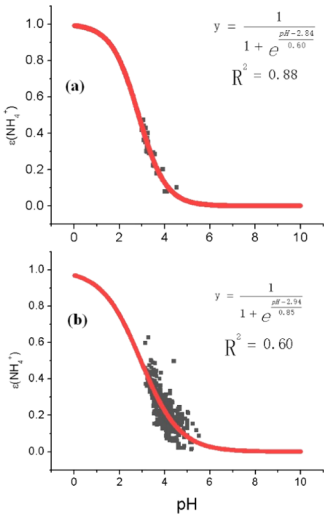

Figure 3. (a) Boltzmann fitting results for the summer sample: $\varepsilon(NO_3^-)$* constrained from 0.7 to 0.8; (b) Boltzmann fitting results for all three season (spring, summer, and winter) samples within a certain range of $\varepsilon(NO_3^-)$* (0.8−0.95) and RH (>36%). Reversed-S curve constructed by fitting $\varepsilon(NH_4^+)$ as a function of pH using the Boltzmann equation for summer samples. The black points are actual atmospheric samples with a certain range of $\varepsilon(NO_3^-)$*; red points are calculated by the Boltzmann equation. $\varepsilon(NH_4^+)$ was calculated using measured NH_4^+ concentration in the particle phase and measured NH_3(g) concentration in the gas phase.

methods or materials. The above statistical analysis confirmed that a Reversed-S curve can be found for the ambient data set in summer. We have also tried to constrain other parameters, but the results were not as satisfactory as constraining $\varepsilon(NO_3^-)$*.

Thermodynamic Analysis for pH, Meteorological Condition, $\varepsilon(NH_4^+)$, and $\varepsilon(NO_3)$*. We also performed a thermodynamic analysis to analyze the Reversed-S curve of pH−$\varepsilon(NH_4^+)$ for the ambient data set and to demonstrate how the above-discussed factors impact $\varepsilon(NH_4^+)$.

As shown in the previous literature,[12] the gas-particle partitioning of NH_4^+ and pH follows a theoretical relationship as described in eq 5

$$\varepsilon(NH_4^+) = \frac{10^{-6} H^*_{NH_3} RTL}{1 + 10^{-6} H^*_{NH_3} RTL} \quad (5)$$

where $H^*_{NH_3}$ is the effective Henry law constant for NH_3 in M atm^{-1} ($H^*_{NH_3}$ value at 293 K is calculated by equations that can be found in Clegg and Brimblecombe and Clegg et al.);[65,66] R is the ideal-gas constant equal to 0.08205 atm L mol^{-1} K^{-1}; T is the temperature in K; and L is the aerosol liquid water content in g m^{-3} (in this work, the water content was estimated by ISORROPIA-II). It should be noted that for eq 8, abundant water is available to dissolve NH_3.[12]

The partitioning of ammonium between gaseous and aqueous phases can be calculated using the effective Henry's law constant for ammonia. So, the ambient ammonia data set can be calculated by eq 6

$$H^*_{NH_3} = \frac{H_{NH_3} K_{a1} [H^+]}{K_w} \quad (6)$$

https://dx.doi.org/10.1021/acs.est.9b07302
Environ. Sci. Technol. 2020, 54, 9834−9843

where H_{NH_3} is the Henry law constant for NH_3; K_{a1} is the equilibrium constant of the reaction $NH_3{\cdot}H_2O \rightleftharpoons NH_4^+ + OH^-$; and K_w is the dissociation constant of water.[12] All of these constants are influenced by temperature. Thus, for different seasons, the values of these constants should be calculated individually. The average daily summertime temperatures in Tianjin range from about 295 to 308.5 K, with an average of 301 K and a standard deviation of 2.78 K. In this study, we calculated thermodynamic constants at 301 K, leading to $H_{NH_3} = 54.04$ M atm^{-1}, $K_{a1} = 1.73 \times 10^5$, and $K_w = 1 \times 10^{-13.90}$, recognizing they are temperature-dependent.

In our previous work,[9] we established an $I_{TL}^{HNO_3}$ index to analyze the thermodynamics for the S curve of pH−$\varepsilon(NO_3^-)$; similarly, we also established an $I_{TL}^{NH_3}$ index here to explore the thermodynamics for the Reversed-S curve of pH−$\varepsilon(NH_4^+)$. In this work, we define $10^{-6}H_{NH_3}^{*}RTL/[H^+](H_{NH_3}^{*} \approx 7.45 \times 10^{10} \times [H^+]$ at 301 K, the average temperature in summer) as the index $I_{TL}^{NH_3}$ and we obtain eq 7

$$\varepsilon(NH_4^+) = \frac{I_{TL}^{NH_3}}{\frac{1}{[H^+]} + I_{TL}^{NH_3}} \tag{7}$$

Equation 7 shows the relationship between $\frac{1}{[H^+]}$, $I_{TL}^{NH_3}$, and $\varepsilon(NH_4^+)$. The equation can clearly describe the Reversed-S curve on the pH−$\varepsilon(NH_4^+)$ plot: when $I_{TL}^{NH_3}$ is close to 0, $\frac{1}{[H^+]}$ is greater than 100, and $\varepsilon(NH_4^+)$ will be close to 0 (lower band); when $I_{TL}^{NH_3}$ approaches ∞, $\varepsilon(NH_4^+)$ will be close to 1 (upper band); when the values of $I_{TL}^{NH_3}$ and $\frac{1}{[H^+]}$ are similar, $\varepsilon(NH_4^+)$ is sensitive to both of $I_{TL}^{NH_3}$ and $\frac{1}{[H^+]}$ (sensitive band). Therefore, when $I_{TL}^{NH_3}$ is constrained within a certain range, an obvious Reversed-S curve of pH-$\varepsilon(NH_4^+)$ would appear. For example, in the summer of this work, $[H^+]$ was in the range of 0.000001 to 0.01 M (pH approximately from 2 to 6); $\varepsilon(NH_4^+)$ is sensitive to $[H^+]$, as $I_{TL}^{NH_3}$ ranging from 0.92×10^2 to 4.19×10^5 is not significantly different from $1/[H^+]$ (about 10^2−10^6). When pH is greater than 6, $1/[H^+]$ is much higher than the maximum value of $I_{TL}^{NH_3}$ (4.19×10^5), and the effects of varying T and L on $\varepsilon(NH_4^+)$ can be ignored; while pH is less than 2, $1/[H^+]$ is much lower than the minimum value of $I_{TL}^{NH_3}$ (0.92×10^2); hence the variation of ambient T and L would greatly influence $\varepsilon(NH_4^+)$. Additionally, when pH is between 2 and 6, both $[H^+]$ and $I_{TL}^{NH_3}$ can impact $\varepsilon(NH_4^+)$.

In this work, $I_{TL}^{NH_3}$ (calculated by eq 7, $H_{NH_3}^{*} \approx 7.45 \times 10^{10} \times [H^+]$ at 301 K, average temperature in summer) ranged from 0.92×10^2 to 4.19×10^5, with an average of 6.12×10^4 in summer. This range dwarfs the impact of the temperature variation on Henry's law constants. However, to better understand the influence of T, we have added a sensitivity regime map (Figure S12) showing how temperature impacts the relationship between LWC and pH.

In our previous work,[9] we applied the similar thermodynamic analysis method to analyze the S curve of pH-$\varepsilon(NO_3^-)$, as shown in eq 8

$$\varepsilon(NO_3^-)^{*} = \frac{I_{TL}^{HNO_3}}{[H^+] + I_{TL}^{HNO_3}} \tag{8}$$

where $I_{TL}^{HNO_3}$ is equal to $10^{-6}H_{HNO_3}^{*}RTL[H^+]$.[9,12] Hence, we can obtain eqs 9 and 10

$$I_{TL}^{NH_3} = \frac{\frac{\varepsilon(NH_4^+)}{[H^+]}}{1 - \varepsilon(NH_4^+)} \tag{9}$$

$$I_{TL}^{HNO_3} = \frac{\varepsilon(NO_3^-)^{*}[H^+]}{1 - \varepsilon(NO_3^-)^{*}} \tag{10}$$

Because in this study (in summer), $I_{TL}^{NH_3} = 7.45 \times 10^4 RTL = 3.08 \times 10^4\, I_{TL}^{HNO_3}$,[12] when we compare eqs 9 and 10, we can obtain eq 11

$$\frac{\varepsilon(NH_4^+)(1 - \varepsilon(NO_3^-)^{*})}{(1-\varepsilon(NH_4^+))\varepsilon(NO_3^-)^{*}} = 3.08 \times 10^4[H^+]^2 \tag{11}$$

If we define $k = \frac{I_{TL}^{NH_3}}{I_{TL}^{HNO_3}} = 3.08 \times 10^4$ L^2 mol^{-2},[12] then we obtain the relationship between $\varepsilon(NH_4^+)$ and $\varepsilon(NO_3^-)$ as eqs 12 and 13

$$\varepsilon(NH_4^+) = \frac{k[H^+]^2\varepsilon(NO_3^-)^{*}}{1 - \varepsilon(NO_3^-)^{*} + k[H^+]^2\varepsilon(NO_3^-)^{*}} \tag{12}$$

$$\frac{1}{\varepsilon(NH_4)} = \frac{1 - \varepsilon(NO_3^-)^{*} + k[H^+]^2\varepsilon(NO_3^-)^{*}}{k[H^+]^2\varepsilon(NO_3^-)^{*}} = \frac{1 - \varepsilon(NO_3^-)^{*}}{k[H^+]^2\varepsilon(NO_3^-)^{*}} + 1 \tag{13}$$

Equation 13 shows the relationship between $\varepsilon(NO_3^-)^{*}$ and $\varepsilon(NH_4^+)$: when $\varepsilon(NO_3^-)^{*}$ is close to 1, $\frac{1}{\varepsilon(NH_4)}$ and $\varepsilon(NH_4^+)$ will also be close to 1; when $\varepsilon(NO_3^-)^{*}$ is close to 0, $\frac{1}{\varepsilon(NH_4)}$ will be approaching ∞, while $\varepsilon(NH_4^+)$ will be 0; when the ratio of $(1 - \varepsilon(NO_3^-)^{*})$ to $(k[H^+]^2\varepsilon(NO_3^-)^{*})$ is between 0 and 1, $\varepsilon(NH_4^+)$ is on the sensitive band; and if $\varepsilon(NO_3^-)^{*}$ is similar to $k[H^+]^2$ (because $k[H^+]^2$ usually is a large value), $\varepsilon(NO_3^-)^{*}$ will play an important role in eq 13, which indicates that when $\varepsilon(NO_3^-)^{*}$ changes, $\varepsilon(NH_4^+)$ will change significantly. Thus, when $\varepsilon(NO_3^-)^{*}$ is constrained within a certain range (related to $k[H^+]^2$), an obvious Reversed-S curve of pH−$\varepsilon(NH_4^+)$ would appear.

Therefore, eq 13 can be used to explain the results of Figure 3a. For the samples in Figure 3a, $\varepsilon(NO_3^-)^{*}$ was constrained within 0.7−0.8 and the samples are clustered within the region of pH between 2.5 and 3.5. In this situation, the values of $k[H^+]^2$ (about 10^{-3}−10^{-1}) and $\varepsilon(NO_3^-)^{*}$ (10^{-2}) are similar to each other, and $\varepsilon(NH_4^+)$ is on the sensitive band, suggesting that $\varepsilon(NO_3^-)^{*}$ plays an important role in affecting $\varepsilon(NH_4^+)$. As expected, the fitted equation explained the Reversed-S curve ($R^2 = 0.88$) well.

To further validate the conclusion of the above thermodynamic analysis, the relationships between pH and $\varepsilon(NH_4^+)$ for three season data sets (summer, spring, and winter) were also investigated in this work. The seasonal data set was from the previous work.[9] We combined the samples of the three seasons (spring, summer, and winter) to investigate the pH−$\varepsilon(NH_4^+)$. The samples with RH larger than 36% (larger than 35.0%, the value of efflorescence relative humidity for pure $(NH_4)_2SO_4$) and $\varepsilon(NO_3^-)^{*}$ from 0.8 to 0.95 were selected for Boltzmann fitting. When $\varepsilon(NO_3^-)^{*}$ values were between 0.8 and 0.95, the pH of the selected samples was within 3−4.5. So, the $k[H^+]^2$ is (10^{-5}−10^{-2}), which overlaps the range of $\varepsilon(NO_3^-)^{*}$ (10^{-3}−10^{-2}). The fitted regression equation is

https://dx.doi.org/10.1021/acs.est.9b07302
Environ. Sci. Technol. 2020, 54, 9834−9843

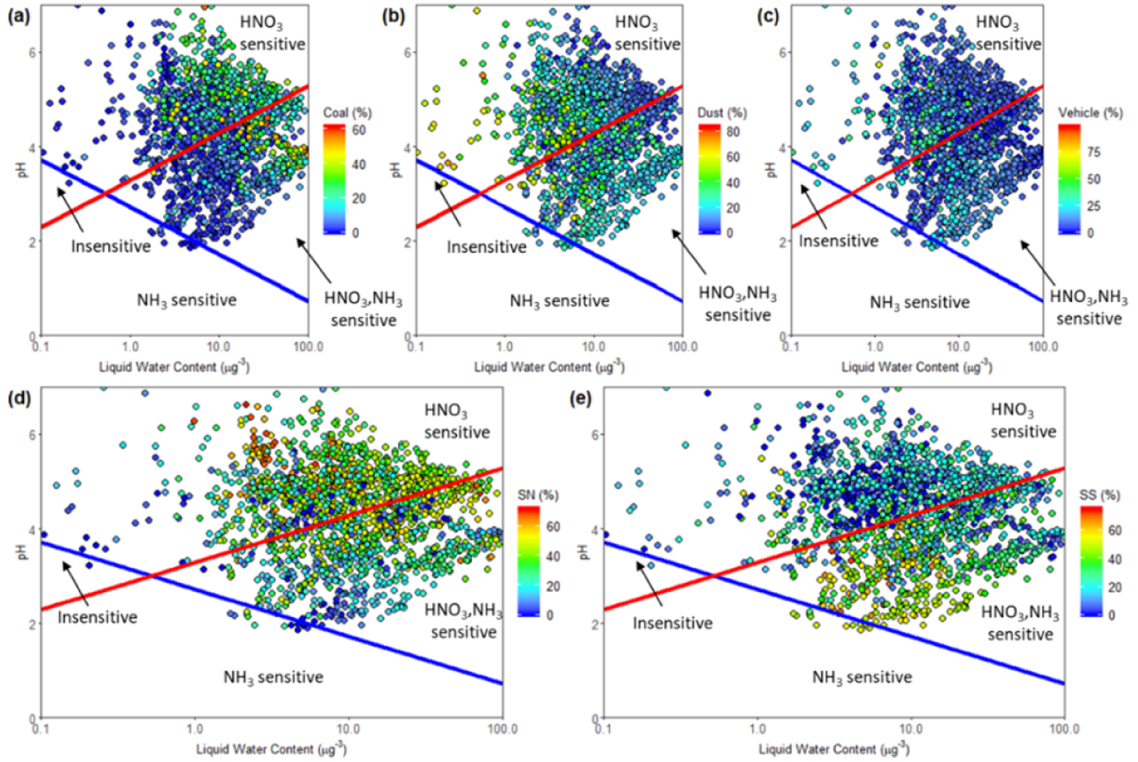

Figure 4. Joint source-NH_3/HNO_3 sensitivity of aerosol pH to NH_3 and HNO_3 for samples from the entire sampling period. (a) Coal, (b) dust, (c) vehicle, (d) SN, and (e) SS.

$$\varepsilon(NH_4^+) = \frac{1}{1 + e^{pH-2.94/0.85}},\ R^2 = 0.60 \quad (14)$$

The fitting result shown in Figure 3b corresponded with our analysis above, which indicated that we could find the Reversed-S curve relationship between $\varepsilon(NH_4^+)$ and pH in ambient dataset.

Additionally, we further investigated the relationship among pH, $\varepsilon(NH_4^+)$, and $\varepsilon(NO_3^-)$ using the "Sensitivity regime map" as developed by Nenes et al.[13] The sensitivity regime map can reflect the domains of the sensitivity of aerosol to NH_3 and HNO_3 availability, in light of the aerosol pH and liquid water content. A detailed description of the map is available elsewhere.[13] Figure S11 shows the results of the samples for all years (Figure S11a) and three seasons (Figure S11b–d). The region lines (red and blue lines on the plots) for all years and different seasons were calculated individually. Compared with the other two seasons, there were lesser points in the HNO_3-sensitive area in summer, but in winter and spring (Figure S11c,d), more points were in the HNO_3-sensitive area, suggesting that those $\varepsilon(NO_3^-)$ were less influenced by $\varepsilon(NH_4^+)$. As discussed above, $\varepsilon(NH_4^+)$ is related to $[H^+]$ and $\varepsilon(NO_3^-)$ (as shown in eq 7). Therefore, the map can also explain why the R^2 for the Reversed-S curve of pH−$\varepsilon(NH_4^+)$ for the entire samples (Figure 3b, R^2 = 0.60) was lower than that for only the summer samples (Figure 3a, R^2 = 0.88), as there are more points in the HNO_3- and NH_3-sensitive regions for summer. In addition, we also tested the temperature sensitivity of the maps (Figure S12).

Joint Source-NH_3/HNO_3 Sensitivity Maps. Furthermore, to better understand the impact of sources on secondary nitrate and to design policies for source controlling, the joint source-NH_3/HNO_3 sensitivity regime map (for all samples) was generated and is provided in Figure 4. Different patterns were observed for diverse sources. For the HNO_3-sensitive region, the points were mainly dominated by vehicle, coal, and dust and had a low level of SS. Most of the points were located in the HNO_3-sensitive region, especially for the vehicle source (Figure 4). This pattern implies that these three sources are related to high pH because of the high pH of the HNO_3-sensitive region in this work. Moreover, ammonia can be directly associated to the emission from vehicle and coal combustion;[48,49] while HNO_3 (gas) is not directly emitted from sources, but generated from the secondary formation by NO_x.[5,6] Additionally, it is worth noting that the SS is dominant in the HNO_3- and NH_3-sensitive regions. It may be explained by the fact that high SS contributes to acidity and liquid water content (LWC) together with the other nonvolatile species and semivolatile species, leading to low nitrate at low pH; in addition, high SS means NH_3 were consumed by sulfate. So, when vehicle and coal dominate, NH_3 usually is rich and the HNO_3 is sensitive to NH_4NO_3 (when SS is low); but in the HNO_3- and NH_3-sensitive region, although some points have high coal and vehicle impacts, the NH_3 is still sensitive to NH_4NO_3 (lots of NH_3 were consumed by high sulfate). Additionally, seasonal (summer, spring, and winter) joint source-NH_3/HNO_3 sensitivity regime maps were also generated (Figures S13–S15). Compared to the summer, in which season most of the points are located in the NH_3- and HNO_3-sensitivity range, spring and winter have more points located in the HNO_3-sensitivity range. This reflects that NH_3 levels were higher relative to other species in the spring and winter than in summer. The HNO_3-sensitive region is mostly dominated by coal, dust, or vehicle source impacts for the three seasons. We also highlighted the points in the Boltzmann fitting plot that were found to have a tendency to be parallel with the blue line (Figure S16). A detailed discussion and

https://dx.doi.org/10.1021/acs.est.9b07302
Environ. Sci. Technol. 2020, 54, 9834−9843

explanation can be found in Supporting Text II of the Supporting Information.

IMPLICATIONS

Compared with the laboratory experiments, the chemistry of ambient aerosol is more complex, due to the presence of other influencing factors such as the variations of meteorological conditions (T and RH) and the behavior of source emissions. Despite the complex processes, the Reversed-S curve between pH and $\varepsilon(NH_4^+)$ can still be found in the hourly ambient aerosol data set, which is similar to that in the laboratory experiments under certain conditions. The Reversed-S curve provides a way for us to better understand the behavior of ammonia and ammonium, under different pH and meteorological (T and RH) levels. It also explains why pH does not increase significantly under an ammonia-rich situation. The results suggest that the thermodynamic model still works for the ambient data set, and certain phenomena occurring in the ambient atmosphere can also be described by the classical thermodynamic theory.

This work also revealed that the partitioning of ammonium can be influenced by the partitioning of nitrate and pH. It shows that when the values of $k[H^+]^2$ and $\varepsilon(NO_3^-)^*$ are similar, $\varepsilon(NH_4^+)$ is dominated by both $k[H^+]^2$ and $\varepsilon(NO_3^-)^*$ (the sensitive band of the Reversed-S curve). In summer, most ambient data are concentrated on the lower pH region, which made the Reversed-S curve more apparent when $\varepsilon(NO_3^-)^*$ is constrained within a certain range. When $\varepsilon(NO_3^-)^*$ of all three seasons' samples were stratified and examined individually, the Reversed-S curve was also apparent. The above findings help us in better understanding the formation of NH_4NO_3 and $(NH_4)_2SO_4$ in the ambient atmosphere. Moreover, such results can also provide important information on controlling particulate matter air pollution. For example, an ammonia control would be effective in the sensitive band of the Reversed-S curve. The results of this study provide insights on controlling ammonia and the impacts of different factors. As revealed in this work, more attention should be focused on H^+ (related to cation/anion emissions) and $NO_3^-/HNO_3(g)$ (related to NO_x emissions) in summer. The theoretical relationship ($k[H^+]^2$ and $\varepsilon(NO_3^-)^*$) (eqs 7 and 13) developed in this work can help in analyzing the gas-particle partitioning of ammonia−ammonium observed in other regions. Also, the sensitivity regime map is found to be a good method to explore the relationship between pH, $\varepsilon(NH_4^+)$, and $\varepsilon(NO_3^-)$, and the results of the map suggested that the impact of seasons should not be overlooked during efforts to control particulate matter air pollution. The joint source-NH_3/HNO_3 sensitivity maps provide a way to identify the dominant source in different sensitive regions and to provide useful information for source control. Additionally, this study is important because we integrated sources, pH and LWC domains, and PM sensitivity to NH_3/HNO_3 emissions all into one map. Through the map, the relationships between primary sources (coal, dust, vehicle, etc.) and secondary aerosols (SN and SS) can be better understood. That is, the key gas species for NH_4NO_3 (sensitive gas) and related sources in different seasons can be better identified. This shows how the effectiveness of controls on gaseous precursor emissions is influenced by pH and meteorological (T and RH) conditions. Regulatory entities can use the maps to help design effective policies to more effectively control nitrate and ammonium aerosol.

ASSOCIATED CONTENT

Supporting Information

The Supporting Information is available free of charge at https://pubs.acs.org/doi/10.1021/acs.est.9b07302.

PMF/ME2 calculation method; Boltzmann fitting patterns in the sensitivity regime maps; theoretical Reversed-S and S curve relationships; factor profiles modeled by PMF/ME2; source contributions' (%) impacts on NH_4^+−$NH_3(g)$ in summer; impact of meteorological conditions, ion activity; Boltzmann fitting curve with RH as color scale; sensitivity regime map for pH, HNO_3, and NH_3; joint source-NH_3/HNO_3 sensitivity (PDF)

AUTHOR INFORMATION

Corresponding Author

Guoliang Shi − *State Environmental Protection Key Laboratory of Urban Ambient Air Particulate Matter Pollution Prevention and Control, Tianjin Key Laboratory of Urban Transport Emission Research, College of Environmental Science and Engineering, Nankai University, Tianjin 300350, P. R. China;* orcid.org/0000-0001-5872-0236; Email: nksgl@nankai.edu.cn

Authors

Qianyu Zhao − *State Environmental Protection Key Laboratory of Urban Ambient Air Particulate Matter Pollution Prevention and Control, Tianjin Key Laboratory of Urban Transport Emission Research, College of Environmental Science and Engineering, Nankai University, Tianjin 300350, P. R. China*

Athanasios Nenes − *School of Architecture, Civil and Environmental Engineering, École Polytechnique Fédérale de Lausanne, Lausanne CH-1015, Switzerland; Institute of Chemical Engineering Sciences, Foundation for Research and Technology Hellas, Patras GR-26504, Greece;* orcid.org/0000-0003-3873-9970

Haofei Yu − *Department of Civil, Environmental and Construction Engineering, University of Central Florida, Orlando, Florida 32816, United States;* orcid.org/0000-0002-7930-8934

Shaojie Song − *School of Engineering and Applied Sciences, Harvard University, Cambridge, Massachusetts 02138, United States;* orcid.org/0000-0001-6395-7422

Zhimei Xiao − *Tianjin Eco-Environmental Monitoring Center, Tianjin 300191, P. R. China*

Kui Chen − *Tianjin Eco-Environmental Monitoring Center, Tianjin 300191, P. R. China*

Yinchang Feng − *State Environmental Protection Key Laboratory of Urban Ambient Air Particulate Matter Pollution Prevention and Control, Tianjin Key Laboratory of Urban Transport Emission Research, College of Environmental Science and Engineering, Nankai University, Tianjin 300350, P. R. China*

Armistead G. Russell − *School of Civil and Environmental Engineering, Georgia Institute of Technology, Atlanta, Georgia 30332-0512, United States*

Complete contact information is available at: https://pubs.acs.org/10.1021/acs.est.9b07302

Notes

The authors declare no competing financial interest.

https://dx.doi.org/10.1021/acs.est.9b07302
Environ. Sci. Technol. 2020, 54, 9834−9843

■ ACKNOWLEDGMENTS

This study was supported by the National Natural Science Foundation of China (41775149), the Tianjin Natural Science Foundation (17JCYBJC23000, 16JCQNJC08700), and the Blue Sky Foundation, Fundamental Research Funds for the Central Universities. No. DQGG0107-03 Air Heavy Pollution Cause and Control Project, China (No. DQGG0107-03). This publication was developed under Assistance Agreement No. EPA834799 awarded by the U.S. Environmental Protection Agency to Emory University and the Georgia Institute of Technology. It has not been formally reviewed by the EPA. The views expressed in this document are solely those of the authors and do not necessarily reflect those of the Agency. EPA does not endorse any products or commercial services mentioned in this publication. We also thank G. Pevur for her help in preparing the manuscript.

■ REFERENCES

(1) Wu, C.; Wang, G. H.; Wang, J. Y.; Li, J. J.; Ren, Y. Q.; Zhang, L.; Cao, C.; Li, J.; Ge, S. S.; Xie, Y. N.; Wang, X. P.; Xue, G. Y. Chemical characteristics of haze particles in Xi'an during Chinese Spring Festival: Impact of fireworks burning. *J. Environ. Sci.* **2018**, *71*, 179−187.

(2) Yao, X.; Chan, C. K.; Fang, M.; Cadle, S.; Chan, T.; Mulawa, P.; He, K.; Ye, B. The water-soluble ionic composition of PM2.5 in Shanghai and Beijing, China. *Atmos. Environ.* **2002**, *36*, 4223−4234.

(3) Qiao, T.; Zhao, M.; Xiu, G.; Yu, J. Seasonal variations of water soluble composition (WSOC, Hulis and WSIIs) in PM1 and its implications on haze pollution in urban Shanghai, China. *Atmos. Environ.* **2015**, *123*, 306−314.

(4) Hua, Y.; Cheng, Z.; Wang, S. X.; Jiang, J. K.; Chen, D. R.; Cai, S. Y.; Fu, X.; Fu, Q. Y.; Chen, C. H.; Xu, B. Y.; Yu, J. Q. Characteristics and source apportionment of PM2.5 during a fall heavy haze episode in the Yangtze River Delta of China. *Atmos. Environ.* **2015**, *123*, 380−391.

(5) Tian, Y. Z.; Shi, G. L.; Han, B.; Wu, J. H.; Zhou, X. Y.; Zhou, L. D.; Zhang, P.; Feng, Y. C. Using an improved source directional apportionment method to quantify the $PM_{2.5}$ source contributions from various directions in a megacity in China. *Chemosphere* **2015**, *119*, 750−756.

(6) Gao, J.; Peng, X.; Chen, G.; Xu, J.; Shi, G. L.; Zhang, Y. F.; Feng, Y. C. Insights into the chemical characterization and sources of PM2.5 in Beijing at a 1-h time resolution. *Sci. Total Environ.* **2016**, *542*, 162−171.

(7) Keene, W. C.; Pszenny, A. A. P.; Maben, J. R.; Stevenson, E.; Wall, A. Closure evaluation of size-resolved aerosol pH in the New England coastal atmosphere during summer. *J. Geophys. Res.: Atmos.* **2004**, *109*, No. D23307.

(8) Guo, H. Y.; Sullivan, A. P.; Campuzano-Jost, P.; Schroder, J. C.; Lopez-Hilfiker, F. D.; Dibb, J. E.; Jimenez, J. L.; Thornton, J. A.; Brown, S. S.; Nenes, A.; Weber, R. J. Fine particle pH and the partitioning of nitric acid during winter in the northeastern United States. *J. Geophys. Res.: Atmos.* **2016**, *121*, 10355−10376.

(9) Shi, X. R.; Nenes, A.; Xiao, Z. M.; Song, S. J.; Yu, H. F.; Shi, G. L.; Zhao, Q. Y.; Chen, K.; Feng, Y. C.; Russell, A. G. High-resolution data sets unravel the effects of sources and meteorological conditions on nitrate and is gas-particle partitioning. *Environ. Sci. Technol.* **2019**, *53*, 3048−3057.

(10) Nah, T.; Guo, H. Y.; Sullivan, A. P.; Chen, Y. L.; Tanner, D. J.; Nenes, A.; Russell, A. G.; Ng, N. L.; Huey, L. G.; Weber, R. J. Characterization of aerosol composition, aerosol acidity and organic acid partitioning at an agriculture-intensive rural southeastern U. S. Site. *Atmos. Chem. Phys.* **2018**, *18*, 11471−11491.

(11) Vasilakos, P.; Russell, A. G.; Weber, R. J.; Nenes, A. Understanding nitrate formation in a world with less sulfate. *Atmos. Chem. Phys.* **2018**, *18*, 12765−12775.

(12) Seinfeld, J. H.; Pandis, S. N. *Atmospheric Chemistry and Physics: From Air Pollution to Climate Change*, 3rd ed.; John Wiley & Sons: Hoboken, New Jersey, 2016.

(13) Nenes, A.; Pandis, S. N.; Weber, R. J.; Russell, A. Aerosol pH and liquid water content determine when particulate matter is sensitive to ammonia and nitrate availability. *Atmos. Chem. Phys.* **2020**, *20*, 3249−3258.

(14) Huntzicker, J. J.; Cary, R. A.; Ling, C. S. Neutralization of sulfuric acid aerosol by ammonia. *Environ. Sci. Technol.* **1980**, *14*, 819−824.

(15) Mcmurry, P. H.; Takano, H.; Anderson, G. R. Study of the ammonia (gas)-sulfuric acid (aerosol) reaction rate. *Environ. Sci. Technol.* **1983**, *17*, 347−352.

(16) Robbins, R. C.; Cadle, R. D. Kinetics of the reaction between gaseous ammonia and sulfuric acid droplets in an aerosol. *J. Phys. Chem. A* **1958**, *62*, 469−471.

(17) Townsend, T. M.; Allanic, A.; Noonan, C.; Sodeau, J. R. Characterization of sulfurous acid, sulfite, and bisulfite aerosol systems. *J. Phys. Chem. A.* **2012**, *116*, 4035−4046.

(18) Miller, G. C. Ammonia. *J. Chem. Educ.* **1981**, *58*, No. 424.

(19) Bergin, M. H.; Ogren, J. A.; Schwartz, S. E.; Mcinnes, L. M. Evaporation of ammonium nitrate aerosol in a heated nephelometer: implications for field measurements. *Environ. Sci. Technol.* **1997**, *31*, 2878−2883.

(20) Battaglia, M. A.; Douglas, S.; Hennigan, C. J. Effect of the urban heat island on aerosol pH. *Environ. Sci. Technol.* **2017**, *51*, 13095−13103.

(21) Bougiatioti, A.; Nikolaou, P.; Stavroulas, I.; Kouvarakis, G.; Weber, R.; Nenes, A.; Kanakidou, M.; Mihalopoulos, N. Particle water and pH in the eastern Mediterranean: source variability and implications for nutrient availability. *Atmos. Chem. Phys.* **2016**, *16*, 4579−4591.

(22) Fountoukis, C.; Nenes, A. ISORROPIA II: a computationally efficient thermodynamic equilibrium model for K+-Ca2+-Mg2+-NH4+-Na+-SO_4^{2-}-NO_3^--Cl−H2O aerosols. *Atmos. Chem. Phys.* **2007**, *7*, 4639−4659.

(23) Clegg, S. L.; Brimblecombe, P.; Wexler, A. S. Thermodynamic model of the system H+-NH4+-SO42−NO_3^--H2O at tropospheric temperatures. *J. Phys. Chem. A.* **1998**, *102*, 2137−2154.

(24) Guo, H. Y.; Liu, J.; Froyd, K. D.; Roberts, J. M.; Veres, P. R.; Hayes, P. L.; Jimenez, J. L.; Nenes, A.; Weber, R. J. Fine particle pH and gas−particle phase partitioning of inorganic species in Pasadena, California, during the 2010 CalNex campaign. *Atmos. Chem. Phys.* **2017**, *17*, 5703−5719.

(25) Parworth, C. L.; Young, D. E.; Kim, H.; Zhang, X.; Cappa, C. D.; Collier, S.; Zhang, Q. Wintertime water-soluble aerosol composition and particle water content in Fresno, California. *J. Geophys. Res. Atmos.* **2017**, *122*, 3155−3170.

(26) Murphy, J. G.; Gregoire, P. K.; Tevlin, A. G.; Wentworth, G. R.; Ellis, R. A.; Markovic, M. Z.; VandenBoer, T. C. Observational constraints on particle acidity using measurements and modelling of particles and gases. *Faraday Discuss.* **2017**, *200*, 379−395.

(27) Yao, X.; Ling, T. Y.; Fang, M.; Chan, C. K. Size dependence of in situ pH in submicron atmospheric particles in Hong Kong. *Atmos. Environ.* **2007**, *41*, 382−393.

(28) Zhang, Q.; Jimenez, J. L.; Worsnop, D. R.; Canagaratna, M. A case study of urban particle acidity and its influence on secondary organic aerosol. *Environ. Sci. Technol.* **2007**, *41*, 3213−3219.

(29) Nenes, A.; Pandis, S. N.; Pilinis, C. ISORROPIA: A new thermodynamic equilibrium model for multiphase multicomponent inorganic aerosols. *Aquat. Geochem.* **1998**, *4*, 123−152.

(30) Meskhidze, N.; Chameides, W.; Nenes, A.; Chen, G. Iron Mobilization in Mineral Dust: Can Anthropogenic SO2 Emissions Affect Ocean Productivity? *Geophys. Res. Lett.* **2003**, *30*, No. 2085.

(31) Fountoukis, C.; Nenes, A.; Sullivan, A.; Weber, R.; Van Reken, T.; Fischer, M.; Matias, E.; Moya, M.; Farmer, D.; Cohen, R. C. Thermodynamic characterization of Mexico City aerosol during MILAGRO 2006. *Atmos. Chem. Phys.* **2009**, *9*, 2141−2156.

https://dx.doi.org/10.1021/acs.est.9b07302
Environ. Sci. Technol. 2020, 54, 9834−9843

(32) Nowak, J. B.; Huey, L. G.; Russell, A. G.; Tian, D.; Neuman, J. A.; Orsini, D.; Sjostedt, S. J.; Sullivan, A. P.; Tanner, D. J.; Weber, R. J.; Nenes, A.; Edgerton, E.; Fehsenfeld, F. C. Analysis of urban gas phase ammonia measurements from the 2002 Atlanta Aerosol Nucleation and Real-Time Characterization Experiment (ANARChE). *J. Geophys. Res.* **2006**, *111*, No. D17308.
(33) Hennigan, C. J.; Izumi, J.; Sullivan, A. P.; Weber, R. J.; Nenes, A. A critical evaluation of proxy methods used to estimate the acidity of atmospheric particles. *Atmos. Chem. Phys.* **2015**, *15*, 2775−2790.
(34) Song, S. J.; Gao, M.; Xu, W. Q.; Shao, J. Y.; Shi, G. L.; Wang, S. X.; Wang, Y. X.; Sun, Y. L.; McElroy, M. B. Fine-particle pH for Beijing winter haze as inferred from different thermodynamic equilibrium models. *Atmos. Chem. Phys.* **2018**, *18*, 7423−7438.
(35) Henry, R. C. Multivariate receptor models-current practice and future trends. *Chemom. Intell. Lab. Syst.* **2002**, *60*, 43−48.
(36) Paatero, P. The multilinear engine-a table-driven, least squares program for solving multilinear problems, including the n-way parallel factor analysis model. *J. Comput. Graph. Stat.* **1999**, *8*, 854−888.
(37) Paatero, P. *End User's Guide to Multilinear Engine Applications*. 2007.
(38) Henry, R. C.; Christensen, E. R. Selecting an appropriate multivariate source apportionment model result. *Environ. Sci. Technol.* **2010**, *44*, 2474−2481.
(39) Guo, H.; Xu, L.; Bougiatioti, A.; Cerully, K. M.; Capps, S. L.; Hite, J. R., Jr.; Carlton, A. G.; Lee, S.-H.; Bergin, M. H.; Ng, N. L.; Nenes, A.; Weber, R. J. Fine-particle water and pH in the southeastern United States. *Atmos. Chem. Phys.* **2015**, *15*, 5211−5228.
(40) Surratt, J. D.; Lewandowski, M.; Offenberg, J. H.; Jaoui, M.; Kleindienst, T. E.; Edney, E. O.; Seinfeld, J. H. Effect of acidity on secondary organic aerosol formation from isoprene. *Environ. Sci. Technol.* **2007**, *41*, 5363−5369.
(41) Surratt, J. D.; Chan, A. W.; Eddingsaas, N. C.; Chan, M.; Loza, C. L.; Kwan, A. J.; Hersey, S. P.; Flagan, R. C.; Wennberg, P. O.; Seinfeld, J. H. Reactive intermediates revealed in secondary organic aerosol formation from isoprene. *Proc. Natl. Acad. Sci. U.S.A.* **2010**, *107*, 6640−6645.
(42) Eddingsaas, N. C.; VanderVelde, D. G.; Wennberg, P. O. Kinetics and Products of the Acid-Catalyzed Ring-Opening of Atmospherically Relevant Butyl Epoxy Alcohols. *J. Phys. Chem. A* **2010**, *114*, 8106−8113.
(43) Myriokefalitakis, S.; Daskalakis, N.; Mihalopoulos, N.; Baker, A. R.; Nenes, A.; Kanakidou, M. Changes in dissolved iron deposition to the oceans driven by human activity: a 3-D global modelling study. *Biogeosciences* **2015**, *12*, 3973−3992.
(44) Pye, H. O. T.; Nenes, A.; Alexander, B.; Ault, A. P.; Barth, M. C.; Clegg, S. L.; Collett, J. L., Jr.; Fahey, K. M.; Hennigan, C. J.; Herrmann, H.; Kanakidou, M.; Kelly, J. T.; Ku, I.; McNeill, V. F.; Riemer, N.; Schaefer, T.; Shi, G. L.; Tilgner, A.; Walker, J. T.; Wang, T.; Weber, R.; Xing, J.; Zaveri, R. A.; Zuend, A. The Acidity of Atmospheric Particles and Clouds. *Atmos. Chem. Phys.* **2020**, *20*, 4809−4888.
(45) Blanchard, C.; Hidy, G.; Tanenbaum, S.; Edgerton, E.; Hartsell, B. The Southeastern Aerosol Research and Characterization (SEARCH) study: Temporal trends in gas and PM concentrations and composition, 1999-2010. *J. Air Waste Manage. Assoc.* **2013**, *63*, 247−259.
(46) Pant, P.; Harrison, R. M. Critical review of receptor modelling for particulate matter: a case study of India. *Atmos. Environ.* **2012**, *49*, 1−12.
(47) Tian, Y.; Liu, J. Y.; Han, S. Q.; Shi, X. R.; Shi, G. L.; Xu, H.; Yu, H. F.; Zhang, Y. F.; Feng, Y. C.; Russell, A. G. Spatial, seasonal and diurnal patterns in physicochemical characteristics and sources of $PM_{2.5}$ in both inland and coastal regions within a megacity in China. *J. Hazard. Mater.* **2018**, *342*, 139−149.
(48) Nah, T.; Guo, H.; Sullivan, A. P.; Chen, Y.; Tanner, D. J.; Nenes, A.; Russell, A.; Ng, N. L.; Huey, L. G.; Weber, R. J. Characterization of aerosol composition, aerosol acidity, and organic acid partitioning at an agriculturally intensive rural southeastern US site. *Atmos. Chem. Phys.* **2018**, *18*, 11471−11491.
(49) Perrino, C.; Catrambone, M.; Di Menno Di Bucchianico, A.; Allegrini, I. Gaseous ammonia in the urban area of Rome, Italy and its relationship with traffic emissions. *Atmos. Environ.* **2002**, *36*, 5385−5394.
(50) Behera, S. N.; Sharma, M.; Aneja, V. P.; Balasubrmanian, R. Ammonia in the atmosphere: a review on emission sources, atmospheric chemistry and deposition on terrestrial bodies. *Envrion. Sci. Pollut. Res. Int.* **2013**, *20*, 8092−8131.
(51) Shi, G. L.; Xu, J.; Peng, X.; Xiao, Z. M.; Chen, K.; Tian, Y. Z.; Guan, X. B.; Feng, Y. C.; Yu, H. F.; Nenes, A.; Russell, A. G. pH of aerosols in a polluted atmosphere: source contributions to highly acidic aerosol. *Environ. Sci. Technol.* **2017**, *51*, 4289−4296.
(52) Han, J.; Morag, C. The influence of the sigmoid function parameters on the speed of backpropagation learning from natural to artificial neural computation. *Lect. Notes Comput. Sci.* **1995**, *930*, 195−201.
(53) Shi, G. L.; Xu, J.; Shi, X. R.; Liu, B. S.; Bi, X. H.; Xiao, Z. M.; Chen, K.; Wen, J.; Dong, S. H.; Tian, Y. Z.; Feng, Y. C.; Yu, H. F.; Song, S. J.; Zhao, Q. Y.; Russell, A. G. Aerosol pH dynamics during intense haze periods in China: Use of detailed, hourly, speciated observations to study the role of ammonia availability and secondary aerosol formation. *J. Geophys. Res. Atmos.* **2019**, *124*, 9730−9742.
(54) Khlystov, A.; Stanier, C. O.; Takahama, S.; Pandis, S. N. Water content of ambient aerosol during the Pittsburgh Air Quality Study. *J. Geophys. Res.* **2005**, *110*, No. D07S10.
(55) Cheng, Y.; Zheng, G.; Wei, C.; Mu, Q.; Zheng, B.; Wang, Z.; Gao, M.; Zhang, Q.; He, K.; Carmicheael, G.; Poschl, U.; Su, H. Reactive nitrogen chemistry in aerosol water as a source of sulfate during haze events in China. *Sci. Adv.* **2016**, *2*, No. e1601530.
(56) Sievering, H.; Boatman, J.; Galloway, J.; Keene, W.; Kim, Y.; Luria, M.; Ray, J. Heterogeneous sulfur conversion in sea salt aerosol particles: the role of aerosol water content and size distribution. *Atmos. Environ., Part A* **1991**, *25*, 1479−1487.
(57) Sun, Y.; Wang, Z.; et al. Primary and secondary aerosols in Beijing in winter: sources, variations and processes. *Atmos. Chem. Phys.* **2016**, *16*, 8309−8329.
(58) Gmehling, J. From UNIFAC to modified UNIFAC to PSRK with the help of DDB. *Fluid Phase Equilib.* **1995**, *107*, 1−29.
(59) Raatikainen, T.; Laaksonen, A. Application of several activity coefficient models to water-organic-electrolyte aerosols of atmospheric interest. *Atmos. Chem. Phys.* **2005**, *5*, 2475−2495.
(60) Zuend, A.; Marcolli, C.; Peter, T.; Seinfeld, J. H. Computation of liquid-liquid equilibria and phase stabilities: implications for RH-dependent gas/particle partitioning of organic-inorganic aerosols. *Atmos. Chem. Phys.* **2010**, *10*, 7795−7820.
(61) Zuend, A.; Seinfeld, J. H. Modeling the gas-particle partitioning of secondary organic aerosol: the importance of liquidliquid phase separation. *Atmos. Chem. Phys.* **2012**, *12*, 3857−3882.
(62) Guo, H.; Otjes, R.; Schlag, P.; Kiendler-Scharr, A.; Nenes, A.; Weber, R. J. Effectiveness of Ammonia Reduction on Control of Fine Particle Nitrate. *Atmos. Chem. Phys.* **2018**, *18*, 12241−12256.
(63) Jamieson, L. E.; Jaworska, A.; Jiang, J.; Baranska, M.; Harrison, D.; Campbell, C. Simultaneous intracellular redox potential and pH measurements in live cells using SERS nanosensors. *Analyst* **2015**, *140*, 2330−2335.
(64) Wei, H. R.; Vejerano, E. P.; Leng, W. N.; Huang, Q. S.; Willner, M. R.; Marr, L. C.; Vikesland, P. J. Aerosol microdroplets exhibit a stable pH gradient. *Proc. Natl. Acad. Sci. U.S.A.* **2018**, *115*, 7272−7277.
(65) Clegg, S. L.; Brimblecombe, P. Equilibrium partial pressures and mean activity and osmotic coefficients of 0-100-percent nitric-acid as a function of temperature. *J. Phys. Chem. B* **1990**, *94*, 5369−5380.
(66) Clegg, S. L.; Brimblecombe, P.; Wexler, A. S. Thermodynamic model of the system H^+-NH_4^+-SO_4^{2-}-NO_3^--H_2O at tropospheric temperatures. *J. Phys. Chem. A* **1998**, *102*, 2137−2154.

https://dx.doi.org/10.1021/acs.est.9b07302
Environ. Sci. Technol. 2020, 54, 9834−9843